Neuron tracing and quantitative analyses of dendritic architecture reveal symmetrical three-way-junctions and phenotypes of *git-1* in *C. elegans*

Omer Yuval[1,2], Yael Iosilevskii[1], Benjamin Podbilewicz[1*], Tom Shemesh[1*]

[1]Faculty of Biology, Technion–Israel Institute of Technology, Haifa 32000, Israel
[2]School of Computing, Faculty of Engineering and Physical Sciences, University of Leeds, United Kingdom
[*]Correspondence: tomsh@technion.ac.il, podbilew@technion.ac.il

Abstract

Complex dendritic trees are a distinctive feature of neurons. Alterations to dendritic morphology are associated with developmental, behavioral and neurodegenerative diseases. The highly-arborized PVD neuron of *C. elegans* serves as a model to study dendritic patterning; however, quantitative, objective and automated analyses of PVD morphology are missing. Here, we present a method for neuronal feature extraction, based on deep-learning and fitting algorithms. The extracted neuronal architecture is represented by a database of structural elements for abstracted analysis. We obtain excellent automatic tracing of PVD trees and uncover that dendritic junctions are unevenly distributed. Surprisingly, these junctions are three-way-symmetrical on average, while dendritic processes are arranged orthogonally. We quantify the effect of mutations in *git-1*, a regulator of dendritic spine formation, on PVD morphology and discover a localized reduction in junctions. Our findings shed new light on PVD architecture, demonstrating the effectiveness of our objective analyses of dendritic morphology and suggest molecular control mechanisms.

Keywords: neuronal structure analysis, dendritic arborization, convolutional neural network, PVD neuron, fitting algorithm, three-way junctions

Author Summary

Nerve cells (neurons) collect input signals via branched cellular projections called dendrites. A major aspect of the study of neurons, dating back for over 100 years, involves the characterization of neuronal shapes and of their dendritic processes.

Here, we present an algorithmic approach for detection and classification of the tree-like dendrites of the PVD neuron in *C. elegans* worms. A key feature of our approach is to represent dendritic trees by a sets of fundamental shape elements, such as junctions and linear sections. By analyzing this dataset, we discovered several novel structural features. We have found that the junctions connecting branched dendrites have a three-way-symmetry, although the dendrites are arranged in a crosshatch pattern; and that the distribution of junctions varies across distinct sub-classes of the PVD's dendritic tree. We further quantified subtle morphological effects due to mutations in *git-1* gene, a known regulator of dendritic spines. Our findings suggest molecular mechanisms for dendritic shape regulation and may help direct new avenues of research.

Introduction

The link between the information processing function of neurons and the intricate shapes of their dendritic processes has been the subject of over a century of extensive study [1–3]. Morphological features of dendritic arbors, such as length, diameter, and orientation have been related to neuronal functions [4–12], while deformations of the dendritic architecture have been associated with diseases and disorders [13–18]. Dendritic morphology varies

significantly across species and across neuronal classes, which are often associated with individually characteristic shapes [2,3,19–21].

Over the past decade, the *C. elegans* bilateral PVD neuron has become a powerful model to study dendritic patterning, owing greatly to its stereotypical, highly ordered structure in the fourth larval stage and young adult (Fig. 1A) [22]. The PVD neuron is located between the hypodermis and its basement membrane [22,23], and functions as a polymodal nociceptor, a mechano- and thermo-sensor, and was suggested to play a role in proprioception – the sensing of body posture [23–25]. Two PVD cell bodies are born post-embryonically in the second larval stage (L2) and develop across the last three larval stages before adulthood (L2-L4), by a dynamic process of dendritic growth and retraction. By late L4 (typically within ~30 hours at 20°C), their complex dendritic arbor of repeating candelabra-shaped units extends almost the entire surface area of the worm [22–24]. This highly organized structure is made of tubular processes with diameters ranging between 35-60 nm [22,23,26]. Studies have implicated the PVD in a variety of functions, including self-fusion, aging and regeneration, and more recently for exploring structural aspects of neuropsychiatric and neurodegenerative diseases [22,27–31]. The relatively complex and high-order arborization of the PVD makes it an excellent model for studying the connection between structure and function in the nervous system [22,23,32,33].

A known regulator of dendritic morphogenesis and synaptic plasticity is GIT1: a GTPase activating protein for the small GTPase Arf (ADP ribosylation factor), as well as a focal adhesion scaffolding protein. Mutations in GIT1 have been linked with fear response and learning impairment, as well as reduced motor coordination and altered walking gait in rodents [34,35]. It has also been implicated in Huntington's disease, Schizophrenia, and Attention Deficit and Hyperactivity Disorder (ADHD) [36–39], reviewed in (Zhou et al, 2016). Moreover, PIX (p21-activated kinase [PAK]-interacting exchange factor), the most prominent

binding partner of GIT1, has been implicated in mental retardation in humans [40]. Several studies in rodent models have identified a link between GIT1 and a reduction in the number of dendritic spines [34,41,42] and a recent report suggests it may have a structural role in the PVD as well [43].

Analysis of neuron architecture faces two fundamental challenges; foremost of which is the extraction of cellular features from microscopy images [44–46]. Due to the inherent noise associated with optical microscopy of living systems, identifying and isolating the relevant image portions is a technically difficult and error-prone process [47–50]. Following segmentation, there remains the second challenge of interpreting and analyzing the segmented structures. As neurons display elaborate and varied shapes, characterization of their morphologies requires complex metrics and classifications, often developed or adjusted for a specific cell type [8–10]. In particular, the dendritic arbors of PVD neurons are described in terms of visually-striking, repetitive morphological elements, referred to as 'menorahs' or multibranched candelabra [22,32,51] (Fig. 1B-C). Characterization of the PVD dendritic morphology is therefore accomplished by annotation and quantification of the menorah structure (Fig. 1C). Due to the intricacy of these challenges, both extraction and analysis of PVD morphology are usually performed semi-manually, using time-consuming methods that prohibit large-scale studies. In addition, human characterization of neuronal shapes is highly subjective and often not sensitive enough for subtle, small-scale structures, raising the need for a high-precision, unbiased, quantitative analysis of morphological features [22,27,51,52]. While multiple image-processing tools are utilized to assist in tracing of neuronal elements [47–50,53], most methods do not easily lend themselves to post-tracing quantitative analysis. Moreover, general-use segmentation algorithms do not consider how the geometry of the neuronal processes is related to the overall shape of the *C. elegans* organism. An integrated

tool that combines detection, segmentation and analysis of the PVD's dendritic tree is therefore required.

Here, we present a computational tool for the automated segmentation and analysis of PVD neuronal architecture. Tracing neuronal processes from microscopy data is performed by a hybrid algorithm, combining a region-based active-contour model for feature extraction [54–58], with a deep learning network for image filtering [59–64] (Fig. 1D). While the image tracing functions may be assisted by a human operator, segmentation operates in a fully autonomous mode and batch-processes multiple raw microscopy images. Following the tracing step, quantification and classification of the extracted features are performed algorithmically (Fig. 1D). Finally, the tracing and analysis outputs are catalogued, stored and shared in a neuronal morphology database. We utilize the collected morphological data for two tasks: first, by analyzing an extensive set of quantified PVD structures, we aim to update the current histological knowledge of the PVD neuron. This detailed knowledge can afford insight into the underlying mechanisms that sculpt neuronal structures. Further, the morphological database is used to quantify the effect of *git-1* mutation on the *C. elegans* PVD neuron during early adulthood. Thus, also demonstrating the use of the tool for the detection and quantification of subtle morphological differences as a result of mutations that were implicated in human disease.

Results

Extraction of PVD morphology from microscopy data

Deep-learning algorithms are widely used for segmentation of microscopy data in general, and neuronal shapes in particular [61–65]. Here, we designed, trained and applied a convolutional neural network (CNN; Fig. S1) in order to filter fluorescent background noise

and eliminate non-neuronal labeled components such as gut granules [66]. We used the stereotypically arborized PVD neuron of one-day adult *C. elegans* (Fig 1A). The CNN operates on small sub-regions of the image (see Fig. 2A for an ensemble of raw and denoised regions), which are then re-assembled to reconstruct the full image. Next, the processed image is binarized and skeletonized, providing an estimate of the PVD shape (Fig 1D). While the neural network is highly efficient in filtering raw microscopy images, we found that the CNN-derived skeleton is insufficient for a faithful representation of the PVD (see Fig. S2D).

In order to accurately extract the PVD morphology, we employed a simplified region-based active contour model [54–58]. Briefly, active contour methods detect morphological features by optimally fitting predefined shapes to the data. The optimization is influenced by "external forces" that attract the model shape to specific image elements, and "internal forces" that enforce intrinsic properties of the model shape, such as curvature [67,68]. Since the PVD dendrites have a tubular morphology with a slowly varying diameter, we represented the PVD shape by a series of discrete rectangular elements (Fig. 2B; green rectangles). The fit score of each rectangular element (corresponding to the "external energy" of the active contour) is defined as the convolution of a rectangular mask with the image data. The score ranges from 0, corresponding to a mask containing no PVD elements (background, blue; Fig 2G and 2H), to 1 for a mask containing only PVD elements (signal, green; Fig 2G and 2H). The orientation of the dendritic process at each location is found by considering possible deviations from the orientation of the preceding element, where a 0° deviation indicates a locally linear segment (Fig 2C). The optimal orientation is defined as maximizing the mask convolution score (Fig 2C-D). The width of the rectangular mask is fitted at each point along the dendritic process by calculating the characteristic length at which the fit score decays with the rectangle width (Fig. 2E-F; see arrows). Note that the fitted rectangular width does not indicate the actual diameter of the dendritic process, which falls below the resolving power of the microscopy setup, but

rather the apparent fluorescent signal of the processes, which varies significantly throughout the PVD [22]. Once a section of the PVD has been fitted with a mask, the local background intensity in the vicinity of the dendrite is calculated and subtracted from the image data (Fig. 2G-H). Thus, detection of dendritic processes is assisted by the segmentation of neighboring regions. Ultimately, the shape of the dendritic processes is represented by a connected chain of rectangles (Fig. 2B). We regulated the continuity and smoothness of the representative chain ("internal energy" of the active contour) by constraining the orientations and widths of successive rectangles (see SI).

In addition to linear elements, the PVD arbors are characterized by junctions that connect dendritic branches (Fig. 2I). We represented such junctions as circular elements, from which rectangular processes emanate radially. First, the position and size of the junctions are found by optimally fitting a circular mask (Fig. 2J). Next, the dendritic processes that originate from each junction are detected by calculating the convolution score of rectangular masks across a range of orientations around the junction center (Fig. 2K). The maxima of the score for different orientations correspond to the set of junctional angles, $\{\alpha_1, \alpha_2, \alpha_3\}$, that characterize the junction's shape (Fig. 2L-M).

Sequential active contour segmentation is highly sensitive to the choice of the starting point [54,69–73]. We overcame this limitation by utilizing the information contained in the CNN-derived skeleton to initialize and guide the active contour process. First, tips and vertices of the CNN skeleton are detected (pixels connected to either one, or more than two pixels, respectively). Skeletonized vertices serve as markers for dendritic junctions, and are used as the initial guess positions for fitting their shapes. Moreover, during the active contour tracing of the linear dendritic processes (Fig. 2B-H) we require the rectangular tracing elements to contain pixels of the CNN-derived skeleton from the corresponding skeleton segment. This constraint combines the benefits of deep learning and active contour fitting, and prevents

divergence of the tracing into image regions that were classified as non-PVD by the CNN. Finally, we utilized the output of the tracing algorithm, as well as manual corrections, to update and retrain the CNN (see Fig. 1D and SI). This feedback loop between the deep-learning classification module and the model-based fitting module is designed to enable a robust and adaptive extraction of the PVD neuron morphology from noisy images.

The combined application of these segmentation procedures results in a dataset containing the position, dimensions, orientation and connectivity of the rectangular elements. Visual inspection confirms that this data serves as an efficient and faithful representation of the PVD shape (*e.g.* Fig. 2N). The abstracted nature of this representation facilitates post-segmentation analysis and may be used to combine multiple images to form larger datasets.

Analysis of PVD shape

Following feature detection, we turned to construct a quantified characterization of the PVD architecture. In order to relate the structure of the dendritic arbor to the shape of the organism, we first defined an appropriate global system of coordinates. Subsequently, the extracted dataset of morphological elements was used to identify spatial patterns that represent intrinsic motifs of PVD organization. Classification of PVD elements according to such motifs is used to provide an idealized PVD representation, as well as a basis for quantitative comparison between phenotypes.

PVD coordinate system

It is convenient to describe the position of the extracted rectangular PVD elements by the natural coordinate system for *C. elegans*, defined by the moving frame $\left(\hat{S},\hat{D},\hat{R}\right)$; where $\hat{S}$ is locally tangential to the worm's longitudinal axis, $\hat{D}$ points along the local dorsal direction, and $\hat{R}$ completes the orthonormal set by pointing in the direction of the worm's right (see Fig. 3A). The worm's longitudinal axis is detected by morphological dilation and erosion image operations (see Fig. 3B, S3B and SI for details).

Since the PVD lies close to the worm surface, positions of its dendritic elements may be given by only two coordinates: distance s along the longitudinal axis (defined as positive posteriorly towards the tail, with the origin anteriorly at the head; A-P in Fig. 3A, 3A-B and S3B), and the azimuth angle ϕ relative to the $\hat{R}$ axis (defined as positive for a counter-clockwise rotation about $\hat{S}$, such that azimuth is positive for dorsal elements, and negative for ventral; see Fig. 3C). Although the worm surface is curved, microscopy images are projected to the flat image plane defined by $\hat{S}$ and $\hat{D}$ vectors. Coordinates of an element in the image plane are therefore given by the distances (s,d), and the transformation between the image and the worm coordinates is given by $\phi = sin^{-1}(d / r(s))$, where $r(s)$ is the radius of the worm at each point along the longitudinal midline axis. For each element of the dendrites, we defined the midline orientation angle θ relative to the local longitudinal axis: $\theta = tan^{-1}(dD / dS)$, where dD and dS are length components in the $\hat{D}$ and $\hat{S}$ directions respectively (see Fig. 3D).

Classification of PVD processes

Based on these definitions, we characterized the spatial distribution of PVD dendrites. We found that PVD elements are spread non-homogeneously in the azimuthal direction, and are predominantly localized at azimuths $\phi \approx 0^{\circ}$ and $\phi \approx \pm 35^{\circ}$ (Fig. 3E-F). The distribution of dendritic processes was found to be symmetrical about the longitudinal midline. As worms were oriented on their sides in all images, the peak at an azimuth of $\phi \approx 0^{\circ}$ corresponds to elements of the PVD's primary branch, while elements belonging to secondary, tertiary and quaternary branch orders are located at progressively increasing $|\phi|$ (Fig. 3E-F). Visual inspection of color-coded PVD segments in specific worms further indicates a correspondence between azimuthal angles and branch orders (Fig. 3E). Next, we examined the local orientation of dendritic processes, θ. Our analysis showed that the distribution of the orientation angles is heterogenous throughout the PVD, yet is roughly symmetric with respect to the longitudinal axis (Fig. 3G-H). We found that dendrites are most likely to locally orient either parallel to the worm axis ($\theta = 0^{\circ}$; red), or normal to it ($\theta = 90^{\circ}$; green) (Fig. 3H). Visual inspection of the orientational distribution showed that PVD elements form a network with rectangular appearance, where connected segements are mostly perpendicular to each other (Fig. 3G-H).

Following these observations, we tested whether there is a correlation of local midline orientation, θ, of dendritic processes with their azimuthal position, ϕ. By plotting the distribution of dendritic elements vs. both azimuth and orientation, we found that PVD elements are strikingly clustered into distinct classes (Fig. 4A). As the clusters were roughly symmetric about the midline, we grouped together dorsal and ventral classes (corresponding to the same magnitudes of azimuthal angles), resulting in four morphological classes (Fig. 4A-C). We found that the classification of complete PVD segments of individual worms according to the most abundant class in each segment closely corresponds to conventional manual

classification of menorah orders by visual inspection (see Fig. 4C and Fig. 1C) [22,23,27]. In order to relate our analysis to earlier works, we named the morphological classes according to the conventional menorah branch order terminology: class-1 (corresponding to primary branch), class-2 (secondary), class-3 (tertiary) and class-4 (quaternary). Importantly, the algorithmically derived classes are similar, but not identical to the menorah ordering scheme described previously [22], (see Fig. S4A). While noting this potential disparity, we found that the consistency and robustness of the algorithmic classification provide an unbiased and reproducible annotation of the PVD dendrites in the wild-type L4 or young adult (see Fig S4B-J for more examples). For an ideal candelabrum (as in Fig. 1C) the orders and classes are usually synonymous. However, branches that differ from the idealized shape are typically labeled as ectopic by manual classification, while the algorithm classifies all branches as belonging to the most similar morphological class.

Using the derived classifications, we next quantified how the total length of PVD dendrites is allocated to the different morphological classes (Fig. 4A). We found that almost half of the PVD processes length is made up of class-4 branches (Fig. 4B and 4C; yellow). We further examined the relative contribution of different morphological classes at differrent positions along the worm's longitudinal (A-P) axis resulting in a schematic of a typical PVD morphology (Fig. 4D). As expected, we found that class-1 processes are located near the longitudinal midline axis (red), and appear uniformly distributed along the head-tail axis. In agreement with previous works [27] PVD sections belonging to higher order classes become more prominent near the cell body, and taper towards its ends .

Finally, we computed the curvature for all PVD elements, and compared the averaged value of the unsigned curvature for different classes. We found that the mean curvature of class-3 elements is significantly higher than class-1 and class-2, whereas class-4 elements are significantly more curved than classes 1-3 (Fig. 4E). Visual inspection of a PVD color-coded

for curvature confirms these results (Fig. 4F). In particular, class-4 segments at the anterior and posterior ends of each mernoah often contain a highly curved region that gives rise to an L-shaped segment (Fig. 4F). These results raise the possibility that by including additional metrics, such as line curvature, the classification of PVD elements may be further enhanced.

Three-way junctions' angles are symmetric on average

Our analysis has shown that PVD junctions connect segments that are, on average, perpendicular to each other. In order to test whether this arragment results from forces that orient the dendritic processes or from intrisic properties of the dendritic junctions, we analyzed the geometry of individual junctions. We found that PVD processes are predominantly connected by 3-way junctions (98.3% of all junctions), while 4-way junctions are scarce (1.7% of all junctions), and higher order junctions were not detected. Next, we determined the relative orientations of the dendritic processes at the points of their connection to the junctions. We observed that each 3-way junction is characterised by an ordered triplet of angles $\{\alpha_1, \alpha_2, \alpha_3\}$, where $\alpha_1 \leq \alpha_2 \leq \alpha_3$ and $\alpha_1 + \alpha_2 + \alpha_3 = 360^\circ$ (see Fig. 5A for examples). Note that, in general, the junction angles differ from the orientations of the processes to which they are connected (see Fig. S5A). After correcting for the distortion of the junction angles due to projection to the image plane (see Fig. 3B-C and SI for details), we found the averages for the smallest, intermediate and largest angles to be $\langle \alpha_1 \rangle = 85^\circ$, $\langle \alpha_2 \rangle = 119^\circ$, and $\langle \alpha_3 \rangle = 156^\circ$ (Fig. 5B). Since the angles in a triplet are not independent, the averages of the angle distributions do not correspond to the most abundant junction geometry. In order to reconstruct the charactersitic PVD junction, we used a Monte Carlo algorithm to simulate a range of possible junction geometries under deformation by random noise (see Fig. 5C, S5B and SI for details). In order to find the angles triplet and the angle variation that best characterize PVD junctions, we fitted the angle distributions of the simulated junctions with the experimentally determined

distributions (Fig. 5D-E; nondimensional fit residuals shown as function of only α_1 and α_2, since $\alpha_3 = 360^\circ - \alpha_1 - \alpha_2$). Angle triplets with lower residual errors indicate a better match with the experimental distributions. Importantly, our analysis shows that the experimental data is in best agreement with junction configurations close to the symmetric $\alpha_1 = \alpha_2 = \alpha_3 = 120^\circ$ shape (Fig. 5D). Moreover, the fit with the simulation reveals that the PVD junctions are somewhat varied: we found that junction angles are distributed around the symmetric cofiguration with a standard deviation of $\sigma_\alpha = 19^\circ$ (see Fig. S5B; showing the fitted angle standard deviation, σ_α, as a function of α_1 and α_2). While this variability of the junction angles allows for intrinsic junction configurations that may deviate from perfect three-way symmetry, these results demonstrate that the orthogonal arrangement of the PVD dendritic arbors (Fig. 1C and 4A) is not a consequence of boundary conditions imposed by PVD junctions, but is rather determined by factors that align the processes themselves. The variability of junction geometry further indicates some mechanical flexibility of the junction structure. These findings may be used to guide future works in the search for the physical mechanisms that shape dendritic junctions.

Distribution of network elements in WT and in *git-1* mutant

We next applied our quantitative morphological approach in order to characterize the role of GIT-1, a known regulator of dendritic spines, in shaping the PVD morphology. In order to quantify the effect of GIT-1, we extracted and analysed the PVD dendritic arbor for *git-1(ok1848)* mutant worms, utilizing the algorithm described for wild-type (WT) worms above (Figs. 6A and S6A-I). As the most elementary metric for comparison, we quantified the length of dendritic process detected in each worm. We found that the average total dendritic length was not affected in the mutant, with $3000 \pm 280\,\mu m$ (n=10), compared to $2900 \pm 270\,\mu m$ in wild-type worms (n=11). Next, we determined how PVD dendrites are distributed into the

previously defined morphological classes. We found that while the total length of PVD dendrites remain unchanged, its distribution into the classes was altered: the combined length of class-4 branches was decreased in the *git-1* mutant compared to WT, whereas the length of class-3 was increased (see Fig 6B). Conversely, we found that the lengths of classes 1and 2 were not changed considerably.

Next, we investigated the effect of *git-1* mutation on the degree of arborization of the PVD dendrites. We define the one-dimensional junction density, ρ , as the number of three-way-junctions per unit length of the dendrites. The junction density is the reciprocal of the mean dendritic distance between neighboring junctions, and therefore constitutes a fundamental structural parameter of the PVD. We found that the overall density of junctions in the PVD of WT worms is $0.047 \pm 0.006\ \mu m^{-1}$, and is unchanged in *git-1* mutant worms. Nevertheless, a more detailed analysis revealed that the junction density varies throughout the PVD, with significantly elevated junction densities found in the 2nd class, compared to the 1st and 4th classes (see Fig 6C). This trend was observed both in wild-type and *git-1* mutants; however, our analysis has revealed a significant decrease in junction density of class 3 branches in the *git-1* mutant, as compared to WT (Fig. 6C).

In addition to 3-way junctions and linear segments, the PVD architecture includes dendritic tips which terminate PVD processes. Such tips may represent sites at which applied mechanical forces can promote dendritic elongation or retraction, as well as potential sites of membrane fusion, leading to the formation of new 3-way junctions. We therefore sought to characterize the effect of *git-1* on the number and distribution of terminal PVD branches. We found that the average number of tips in a PVD is 235 ± 6 (n=11 worms) and is essentially unchanged in *git-1* mutants, with 230 ± 7 (n=10 worms). Similarly to junction density, we characterized the density of terminal tips per unit length of PVD for branches of different classes. We found that the tip density in WT worms increases with the class number, with the

highest tip density found at 4th class (Fig. 6D). This result is remarkable in contrast with the junction density, which is lowest at 4th order branches. In *git-1* mutants the absolute number of terminal class-3 tips is increased, and the number of class-4 tips is reduced (fig. 6E). However, this effect may be explained by the corresponding changes in dendritic lengths of these classes (Fig. 6B), and we found no significant change in the tip densities in *git-1* compared to WT PVDs.

While some, but not all, features of the WT and *git-1* morphology can be confirmed by visual inspection and manual quantitative analyses (Fig 6F-I; see Supplementary Information), the reliable detection of such nuanced differences demonstrates the power of our quantitative automated and objective approach. Taken together, these findings indicate a subtle but significant change in the morphology of the PVD in *git-1* worms that is most prominent in tertiary-classed branches.

Discussion

In this work we presented a quantitative approach for morphological characterization of the PVD neuron in *C. elegans*. By combining statistical and rule-based analysis, we were able to automatically segment microscopy images and overcome the noise and artifacts that are inherent to imaging of dendritic arbors. Following image segmentation, our approach enabled the detection and abstraction of the stereotypical orthogonal patterning of PVD processes.

Algorithmic classification of dendritic trees

Our analysis produced a bias-free classification of dendritic classes that corresponds well with the established order classification of PVD branches – yet is not identical to it. The algorithmic classification takes into account position and orientation of dendritic elements, but does not impose other rules, such as connectivity, between branches. Manual classification, on the other hand, is based on a subjective comparison between PVD branches and an idealized

menorah structure (Fig. 1C). Further, our algorithm classifies all PVD elements according to the closest morphological class, and does not consider indeterminate or mixed cases. Conversely, manual annotations include an idiosyncratic "ectopic" qualifier for branch orders, describing a lack of fit with the idealized menorah shape.

Three-way symmetry of PVD junctions generates orthogonal trees

Beyond the ability to automate the inspection of neuronal architecture, our quantitative analysis has uncovered key morphological features that had not been previously detected. We demonstrated that processes are predominantly connected by junctions with a 3-fold symmetry at the branching points. Since PVD processes are, on average, aligned orthogonally in a crosshatch pattern, this unexpected result indicates that the orientation of dendritic processes does not arise from the boundary conditions applied at the junctions, but is rather achieved by factors that act to guide along the length of the processes [74]. Further, our findings imply that symmetrical 3-way junctions represent the mechanically stable junction configuration. This result is in agreement with earlier works that have shown that 3-way junctions represent the minimal energy shape for connecting tubular membrane surfaces [75]. Yet, the observed junction geometry may also be influenced by a local effect of cytoskeletal proteins or membrane coating proteins. Our findings can therefore serve as a basis for further study of the physical mechanism for stabilization of PVD junctions.

PVD junctions are heterogeneously distributed

Our analysis has revealed that the junctions and tips of dendritic processes are not uniformly distributed throughout the PVD. Class-4 branches have the highest number of tips per dendritic length, as might be expected, but also the lowest number of dendritic junctions per length. Conversely, class-2 branches have the highest junction density and the sparsest tip density. How may these findings be understood? Formation of a dendritic spine from an existing process results in an addition of one junction and one tip to the network. Therefore,

modulating the process of spine formation is not expected to result in a disparity between the junction and tip densities. However, fusion of a dendritic tip will increase the junction density and reduce the density of tips, thereby enhancing the tip-junction disparity. These results therefore suggest that dendritic fusion is enhanced near the primary PVD process and diminishes further away from it. The functions of the fusogen EFF-1 in the dynamics of dendritic architecture and maintenance of the trees may explain this phenomenon [22]. Thus, EFF-1-dependent loop formation could be part of the molecular machinery that controls the number of dendritic tips and three-way junctions. Further work is required for detailed analysis of dendritic loops and for determining the factors governing the PVD topology.

Mutation in *git-1* results in class-specific deformation of PVD geometry

We have found that *git-1* mutation results in a subtle deformation of the PVD architecture. No significant differences were detected for the length of the PVD, its curvature, or the relative distribution into morphological classes. However, we found a significant decrease in the density of junctions along class-3 dendritic process in *git-1* mutant worms, relative to WT. Conversely, the density of class-3 tips was found to increase in the mutant, suggesting that *git-1* acts as a negative regulator of tertiary branch arborization. These findings were confirmed by manual analysis, and we conclude that *git-1* is necessary for both morphogenesis and maintenance of dendritic structure in adulthood. The behavioral phenotypes associated with *git-1* were tested by movement analysis and a harsh touch response assay, where we found that two *git-1* mutant alleles displayed increased speed and body wavelength, with one allele also displaying a mild mechanosensory defect (YI and BP, unpublished results). These results open a possibility for a novel GIT-1-mediated dendritic arborization pathway and changes in proprioceptive faculties in *C. elegans*.

Outlook and future directions

The analysis of the PVD morphology was performed on static images, yet afforded clues to dynamical processes that shape the PVD, such as junction formation and tip fusion. However, the autonomous capabilities of the image segmentation and characterization algorithms are uniquely suited for the processing of a time series of images. In future works, we plan to utilize the tools we have developed in order to study the time dependent development and aging of the dendritic arbor, in order to uncover the mechanisms through which the PVD morphology is developed and maintained [27]. The morphological database that stores the abstracted PVD shapes of individual worms is designed to allow for novel analysis and future expansions. In order to facilitate such studies, we have made the source code of the algorithm, including a custom graphical user interface for easy implementation, available as open code. Finally, while the image segmentation and analysis algorithms have been developed specifically for the PVD neuron, they are based upon low level geometrical features, rather than predefined "platonic" concepts of the ideal PVD morphology. Consequently, we expect the approach presented here to be applicable for segmentation and classification of arbors in other neurons, with different characteristic architectures.

Materials & Methods

C. elegans strains and maintenance

Nematode strains were maintained according to standard methods [76,77]. Strains were maintained on NGM plates with 150 µl OP50 bacteria at 20°C. Both N2 (wild-type) and *git-1* animals were transferred into separate plates at the late L4 stage using a dissecting scope ('Christmas tree' stage vulva, appearing at late L4-very early young adult, as confirmed by Nomarski optics), and imaged 24 hours later, being one-day adults. In addition to *C. elegans* strain N2 the following strains were used: CHB392 [*hmnEx133(ser-2prom3::kaede)*] [78], BP709 *[hmnIs133 (ser-2prom3::kaede)*] [28], RB1540 *git-1(ok1848) X,* BP1054 *git-1(ok1848)*

*X; hmnIs133 (ser-2prom3::*kaede). BP1077 *git-1(tm1962) X; hmnEx133(ser-2prom3::kaede). git-1(ok1848)* was generated by the *C. elegans* Gene Knockout Project at the Oklahoma Medical Research Foundation which is part of the International *C. elegans* Gene Knockout Consortium. *git-1(tm1962)* was generated by the National Bioresource Project, Tokyo, Japan, which is part of the International *C. elegans* Gene Knockout Consortium. BP1077 and BP1054 were generated by crossing BP709 with the *git-1* alleles and the genotypes were confirmed by PCR.

Image acquisition

One-day adult hermaphrodites were anaesthetized for >20 minutes in a drop of 0.01% tetramisole in M9 buffer on a 3% agar pad. Images of the PVD neuron in hermaphrodite *C. elegans* were analyzed by Nomarski optics and fluorescence microscopy using a Nikon eclipse Ti inverted microscope equipped with Yokogawa CSU-X1 spinning disk confocal microscope fitted with a 40 X oil Plan Fluor NA=1.3 lens [28]. We used projections of z-stacked confocal images taken at ~0.5-0.6 μm intervals, digitally stored using iXon EMCCD camera (Andor). The acquisition of the images was done using MetaMorph software, utilizing 25% of 488 nm laser intensity, gain of 200 and 300 ms exposure for image acquisition. Then, the multi-dimensional data (in the form of z-stacks) was projected onto a 2D plane using maximal intensity projection using Fiji/ImageJ software (NIH) to produce a 2D grayscale image.

Image preprocessing

Contrast was autocorrected and the whole PVD pieced together from smaller PVD regions using Adobe Photoshop CS version 8.0 (Adobe Inc.), by utilizing the Image-Adjustments-Autocorrect and File-Automate-Photomerge options, respectively.

Statistical analysis

Statistical analysis was performed pairwise using the nonparametric Mann-Whitney U-test (Wilcoxon rank-sum test). P-value significance: ***P < 0.0005, **P < 0.005, *P < 0.05. 11

animals were used for wild-type, and 10 animals were used for *git-1* mutants. Error bars show the standard deviation.

Software

The code was implemented in MATLAB R2020b. The complete project code is available on GitHub: https://github.com/Omer1Yuval1/Neuronalyzer**.**

See Supplementary Information for further details of algorithms and analysis.

Acknowledgements

We thank the *C. elegans* knockout consortium for the *git-1(ok1848)* deletion allele generated by the *C. elegans* Gene Knockout Project at the Oklahoma Medical Research Foundation and *git-1(tm1962)* was generated by the National Bioresource Project, Tokyo, Japan. M. Heiman and C. Yip for CHB392. Some strains were provided by the Caenorhabditis Genetics Center, which is funded by National Institutes of Health Office of Research Infrastructure Programs (P40 OD010440). This work was supported by the Israel Science Foundation (grant 2751/20 to TS and 257/17 to BP).

Author Contributions

TS and BP conceived and directed the project. TS and OY developed the methodology. OY implemented the algorithms, wrote the code and generated the figures. YI performed the microscopy experiments, traced neuronal images, generated and maintained the strains. OY and YI analyzed the data. TS wrote the manuscript with input from all authors.

Conflict of interest

The authors declare that they have no conflict of interests.

References

1. Kweon JH, Kim S, Lee SB. The cellular basis of dendrite pathology in neurodegenerative diseases. BMB Rep. 2017. doi:10.5483/BMBRep.2017.50.1.131
2. Cajal SR. Histología del sistema nervioso del hombre y de los vertebrados. Minist Sanid y Consum Madrid. 1899.
3. White JG, Southgate E, Thomson JN, Brenner S. The structure of the nervous system of the nematode Caenorhabsitis elegans (the mind of a worm). Philos Trans R Soc Lond B Biol Sci. 1986.
4. Vetter P, Roth A, Häusser M. Propagation of action potentials in dendrites depends on dendritic morphology. J Neurophysiol. 2001. doi:10.1152/jn.2001.85.2.926
5. Shepherd GMG, Stepanyants A, Bureau I, Chklovskii D, Svoboda K. Geometric and functional organization of cortical circuits. Nat Neurosci. 2005. doi:10.1038/nn1447
6. Bosch M, Hayashi Y. Structural plasticity of dendritic spines. Current Opinion in Neurobiology. 2012. doi:10.1016/j.conb.2011.09.002
7. Sullivan LF, Warren TL, Doe CQ. Temporal identity establishes columnar neuron morphology, connectivity, and function in a drosophila navigation circuit. Elife. 2019. doi:10.7554/eLife.43482
8. Langhammer CG, Previtera ML, Sweet ES, Sran SS, Chen M, Firestein BL. Automated Sholl analysis of digitized neuronal morphology at multiple scales: Whole cell Sholl analysis versus Sholl analysis of arbor subregions. Cytom Part A. 2010. doi:10.1002/cyto.a.20954
9. Gutierrez H, Davies AM. A fast and accurate procedure for deriving the Sholl profile in quantitative studies of neuronal morphology. J Neurosci Methods. 2007. doi:10.1016/j.jneumeth.2007.02.002
10. Binley KE, Ng WS, Tribble JR, Song B, Morgan JE. Sholl analysis: A quantitative comparison of semi-automated methods. J Neurosci Methods. 2014. doi:10.1016/j.jneumeth.2014.01.017
11. Cuntz H, Forstner F, Borst A, Häusser M. One rule to grow them all: A general theory of

neuronal branching and its practical application. PLoS Comput Biol. 2010. doi:10.1371/journal.pcbi.1000877

12. Yip ZC, Heiman MG. Ordered arrangement of dendrites within a C. Elegans sensory nerve bundle. Elife. 2018. doi:10.7554/eLife.35825

13. Lanoue V, Usardi A, Sigoillot SM, Talleur M, Iyer K, Mariani J, et al. The adhesion-GPCR BAI3, a gene linked to psychiatric disorders, regulates dendrite morphogenesis in neurons. Mol Psychiatry. 2013. doi:10.1038/mp.2013.46

14. Robinson TE, Kolb B. Structural plasticity associated with exposure to drugs of abuse. Neuropharmacology. 2004. doi:10.1016/j.neuropharm.2004.06.025

15. Benarroch EE. Rho GTPases: Role in dendrite and axonal growth, mental retardation, and axonal regeneration. Neurology. 2007. doi:10.1212/01.wnl.0000259588.97409.8f

16. Kemp K, Gray E, Wilkins A, Scolding N. Purkinje cell fusion and binucleate heterokaryon formation in multiple sclerosis cerebellum. Brain. 2012. doi:10.1093/brain/aws226

17. Fernandez-Gonzalez A, La Spada AR, Treadaway J, Higdon JC, Harris BS, Sidman RL, et al. Purkinje cell degeneration (pcd) phenotypes caused by mutations in the axotomy-induced gene, Nna1. Science (80-). 2002. doi:10.1126/science.1068912

18. Herms J, Dorostkar MM. Dendritic Spine Pathology in Neurodegenerative Diseases. Annual Review of Pathology: Mechanisms of Disease. 2016. doi:10.1146/annurev-pathol-012615-044216

19. Jan YN, Jan LY. The Control of Dendrite Development. Neuron. 2003. doi:10.1016/S0896-6273(03)00631-7

20. Purves D, Lichtman JW. Geometrical differences among homologous neurons in mammals. Science (80-). 1985. doi:10.1126/science.3983631

21. Van Pelt J, Uylings HBM. Natural variability in the geometry of dendritic branching patterns. Modeling in the Neurosciences: From Biological Systems to Neuromimetic Robotics. 2005. doi:10.4324/9780203390979_chapter_5

22. Oren-Suissa M, Hall DH, Treinin M, Shemer G, Podbilewicz B. The fusogen EFF-I controls sculpting of mechanosensory dendrites. Science (80-). 2010;328: 1285–1288.

doi:10.1126/science.1189095

23. Albeg A, Smith CJ, Chatzigeorgiou M, Feitelson DG, Hall DH, Schafer WR, et al. C. elegans multi-dendritic sensory neurons: Morphology and function. Mol Cell Neurosci. 2011. doi:10.1016/j.mcn.2010.10.001

24. Way JC, Chalfie M. The mec-3 gene of Caenorhabditis elegans requires its own product for maintained expression and is expressed in three neuronal cell types. Genes Dev. 1989. doi:10.1101/gad.3.12a.1823

25. Chatzigeorgiou M, Yoo S, Watson JD, Lee WH, Spencer WC, Kindt KS, et al. Specific roles for DEG/ENaC and TRP channels in touch and thermosensation in C. elegans nociceptors. Nat Neurosci. 2010. doi:10.1038/nn.2581

26. Dong X, Shen K, Bülow HE. Intrinsic and Extrinsic Mechanisms of Dendritic Morphogenesis. Annu Rev Physiol. 2015. doi:10.1146/annurev-physiol-021014-071746

27. Kravtsov V, Oren-Suissa M, Podbilewicz B. The fusogen AFF-1 can rejuvenate the regenerative potential of adult dendritic trees by self-fusion. Dev. 2017. doi:10.1242/dev.150037

28. Oren-Suissa M, Gattegno T, Kravtsov V, Podbilewicz B. Extrinsic repair of injured dendrites as a paradigm for regeneration by fusion in Caenorhabditis elegans. Genetics. 2017. doi:10.1534/genetics.116.196386

29. Treinin M, Chalfie M. A mutated acetylcholine receptor subunit causes neuronal degeneration in C. elegans. Neuron. 1995. doi:10.1016/0896-6273(95)90231-7

30. Pir GJ, Choudhary B, Mandelkow E, Mandelkow EM. Tau mutant A152T, a risk factor for FTD/PSP, induces neuronal dysfunction and reduced lifespan independently of aggregation in a C. elegans Tauopathy model. Mol Neurodegener. 2016. doi:10.1186/s13024-016-0096-1

31. Lezi E, Zhou T, Koh S, Chuang M, Sharma R, Pujol N, et al. An Antimicrobial Peptide and Its Neuronal Receptor Regulate Dendrite Degeneration in Aging and Infection. Neuron. 2018. doi:10.1016/j.neuron.2017.12.001

32. Inberg S, Meledin A, Kravtsov V, Iosilevskii Y, Oren-Suissa M, Podbilewicz B. Lessons from Worm Dendritic Patterning. Annu Rev Neurosci. 2019. doi:10.1146/annurev-neuro-072116-

031437

33. Hall DH, Treinin M. How does morphology relate to function in sensory arbors? Trends in Neurosciences. 2011. doi:10.1016/j.tins.2011.07.004

34. Menon P, Deane R, Sagare A, Lane SM, Zarcone TJ, O'Dell MR, et al. Impaired spine formation and learning in GPCR kinase 2 interacting protein-1 (GIT1) knockout mice. Brain Res. 2010. doi:10.1016/j.brainres.2009.11.084

35. Hong S-T, Mah W. A Critical Role of GIT1 in Vertebrate and Invertebrate Brain Development. Exp Neurobiol. 2015. doi:10.5607/en.2015.24.1.8

36. Goehler H, Lalowski M, Stelzl U, Waelter S, Stroedicke M, Worm U, et al. A protein interaction network links GIT1, an enhancer of huntingtin aggregation, to Huntington's disease. Mol Cell. 2004. doi:10.1016/j.molcel.2004.09.016

37. Kim MJ, Biag J, Fass DM, Lewis MC, Zhang Q, Fleishman M, et al. Functional analysis of rare variants found in schizophrenia implicates a critical role for GIT1-PAK3 signaling in neuroplasticity. Mol Psychiatry. 2017. doi:10.1038/mp.2016.98

38. Won H, Mah W, Kim E, Kim JW, Hahm EK, Kim MH, et al. GIT1 is associated with ADHD in humans and ADHD-like behaviors in mice. Nat Med. 2011. doi:10.1038/nm.2330

39. Kim H, Kim JI, Kim H, Kim JW, Kim BN. Interaction effects of GIT1 and DRD4 gene variants on continuous performance test variables in patients with ADHD. Brain Behav. 2017. doi:10.1002/brb3.785

40. Ramakers GJA, Wolfer D, Rosenberger G, Kuchenbecker K, Kreienkamp HJ, Prange-kiel J, et al. Dysregulation of Rho GTPases in the αPix/Arhgef6 mouse model of X-linked intellectual disability is paralleled by impaired structural and synaptic plasticity and cognitive deficits. Hum Mol Genet. 2012. doi:10.1093/hmg/ddr457

41. Zhang H, Webb DJ, Asmussen H, Horwitz AF. Synapse formation is regulated by the signaling adaptor GIT1. J Cell Biol. 2003. doi:10.1083/jcb.200211002

42. Zhang H, Webb DJ, Asmussen H, Niu S, Horwitz AF. A GIT1/PIX/Rac/PAK signaling module regulates spine morphogenesis and synapse formation through MLC. J Neurosci. 2005. doi:10.1523/JNEUROSCI.3553-04.2005

43. Aguirre-Chen C, Stec N, Ramos OM, Kim N, Kramer M, McCarthy S, et al. A Caenorhabditis elegans model for integrating the functions of neuropsychiatric risk genes identifies components required for normal dendritic morphology. G3 Genes, Genomes, Genet. 2020. doi:10.1534/g3.119.400925

44. Lanciego JL, Wouterlood FG. A half century of experimental neuroanatomical tracing. Journal of Chemical Neuroanatomy. 2011. doi:10.1016/j.jchemneu.2011.07.001

45. Meijering E. Neuron tracing in perspective. Cytometry Part A. 2010. doi:10.1002/cyto.a.20895

46. Donohue DE, Ascoli GA. Automated reconstruction of neuronal morphology: An overview. Brain Research Reviews. 2011. doi:10.1016/j.brainresrev.2010.11.003

47. Greenblum A, Sznitman R, Fua P, Arratia PE, Oren M, Podbilewicz B, et al. Dendritic tree extraction from noisy maximum intensity projection images in C. elegans. Biomed Eng Online. 2014. doi:10.1186/1475-925X-13-74

48. Kim KM, Son K, Palmore GTR. Neuron image analyzer: Automated and accurate extraction of neuronal data from low quality images. Sci Rep. 2015. doi:10.1038/srep17062

49. Yang J, Hao M, Liu X, Wan Z, Zhong N, Peng H. FMST: an Automatic Neuron Tracing Method Based on Fast Marching and Minimum Spanning Tree. Neuroinformatics. 2019. doi:10.1007/s12021-018-9392-y

50. Rodriguez A, Ehlenberger DB, Hof PR, Wearne SL. Three-dimensional neuron tracing by voxel scooping. J Neurosci Methods. 2009. doi:10.1016/j.jneumeth.2009.07.021

51. Smith CJ, Watson JD, Spencer WC, O'Brien T, Cha B, Albeg A, et al. Time-lapse imaging and cell-specific expression profiling reveal dynamic branching and molecular determinants of a multi-dendritic nociceptor in C. elegans. Dev Biol. 2010. doi:10.1016/j.ydbio.2010.05.502

52. Salzberg Y, Díaz-Balzac CA, Ramirez-Suarez NJ, Attreed M, Tecle E, Desbois M, et al. Skin-derived cues control arborization of sensory dendrites in Caenorhabditis elegans. Cell. 2013. doi:10.1016/j.cell.2013.08.058

53. Schneider CA, Rasband WS, Eliceiri KW. NIH Image to ImageJ: 25 years of image analysis. Nature Methods. 2012. doi:10.1038/nmeth.2089

54. Li C, Kao CY, Gore JC, Ding Z. Minimization of region-scalable fitting energy for image

segmentation. IEEE Trans Image Process. 2008. doi:10.1109/TIP.2008.2002304

55. Lankton S, Tannenbaum A. Localizing region-based active contours. IEEE Trans Image Process. 2008. doi:10.1109/TIP.2008.2004611

56. Vasilkoski Z, Stepanyants A. Detection of the optimal neuron traces in confocal microscopy images. J Neurosci Methods. 2009. doi:10.1016/j.jneumeth.2008.11.008

57. Schmitt S, Evers JF, Duch C, Scholz M, Obermayer K. New methods for the computer-assisted 3-D reconstruction of neurons from confocal image stacks. Neuroimage. 2004. doi:10.1016/j.neuroimage.2004.06.047

58. Wang Y, Narayanaswamy A, Tsai CL, Roysam B. A broadly applicable 3-D neuron tracing method based on open-curve snake. Neuroinformatics. 2011. doi:10.1007/s12021-011-9110-5

59. Lecun Y, Bengio Y, Hinton G. Deep learning. Nature. 2015. doi:10.1038/nature14539

60. LeCun, Y., & Bengio Y. Convolution Networks for Images, Speech, and Time-Series. Handb brain theory neural networks. 1995. doi:10.1007/s13398-014-0173-7.2

61. Li R, Zeng T, Peng H, Ji S. Deep Learning Segmentation of Optical Microscopy Images Improves 3-D Neuron Reconstruction. IEEE Trans Med Imaging. 2017. doi:10.1109/TMI.2017.2679713

62. Zhou Z, Kuo HC, Peng H, Long F. DeepNeuron: an open deep learning toolbox for neuron tracing. Brain Informatics. 2018. doi:10.1186/s40708-018-0081-2

63. Wang H, Zhang D, Song Y, Liu S, Gao R, Peng H, et al. Memory and Time Efficient 3D Neuron Morphology Tracing in Large-Scale Images. 2018 International Conference on Digital Image Computing: Techniques and Applications, DICTA 2018. 2019. doi:10.1109/DICTA.2018.8615765

64. Saberi-Bosari S, Flores KB, San-Miguel A. Deep learning-enabled phenotyping reveals distinct patterns of neurodegeneration induced by aging and cold-shock. BMC Biol. 2020. doi:10.1101/2020.03.08.982074

65. Hartmann J, Wong M, Gallo E, Gilmour D. An image-based data-driven analysis of cellular architecture in a developing tissue. Elife. 2020. doi:10.7554/eLife.55913

66. Hermann GJ, Schroeder LK, Hieb CA, Kershner AM, Rabbitts BM, Fonarev P, et al. Genetic

analysis of lysosomal trafficking in Caenorhabditis elegans. Mol Biol Cell. 2005. doi:10.1091/mbc.E05-01-0060

67. Williams DJ, Shah M. A Fast algorithm for active contours and curvature estimation. CVGIP Image Underst. 1992. doi:10.1016/1049-9660(92)90003-L

68. Chan TF, Vese LA. Active contours without edges. IEEE Trans Image Process. 2001. doi:10.1109/83.902291

69. Kass M, Witkin A, Terzopoulos D. Snakes: Active contour models. Int J Comput Vis. 1988. doi:10.1007/BF00133570

70. Akram F, Garcia MA, Puig D. Active contours driven by difference of Gaussians. Sci Rep. 2017. doi:10.1038/s41598-017-14502-w

71. Huang Y, Liu Z. Segmentation and tracking of lymphocytes based on modified active contour models in phase contrast microscopy images. Comput Math Methods Med. 2015. doi:10.1155/2015/693484

72. Soomro S, Munir A, Choi KN. Hybrid two-stage active contour method with region and edge information for intensity inhomogeneous image segmentation. PLoS One. 2018. doi:10.1371/journal.pone.0191827

73. Li C, Huang R, Ding Z, Gatenby JC, Metaxas DN, Gore JC. A level set method for image segmentation in the presence of intensity inhomogeneities with application to MRI. IEEE Trans Image Process. 2011. doi:10.1109/TIP.2011.2146190

74. Zou W, Dong X, Broederdorf TR, Shen A, Kramer DA, Shi R, et al. A Dendritic Guidance Receptor Complex Brings Together Distinct Actin Regulators to Drive Efficient F-Actin Assembly and Branching. Dev Cell. 2018. doi:10.1016/j.devcel.2018.04.008

75. Shemesh T, Klemm RW, Romano FB, Wang S, Vaughan J, Zhuang X, et al. A model for the generation and interconversion of ER morphologies. Proc Natl Acad Sci. 2014;111: E5243–E5251. doi:10.1073/pnas.1419997111

76. Brenner S. The genetics of Caenorhabditis elegans. Genetics. 1974.

77. Sulston J, Hodgkin J. Methods in the nematode C. elegans. Cold Spring Harbor Laboratory Press. 1988.

78. Yip ZC, Heiman MG. Duplication of a Single Neuron in C. elegans Reveals a Pathway for Dendrite Tiling by Mutual Repulsion. Cell Rep. 2016. doi:10.1016/j.celrep.2016.05.003

Figure legends

Figure 1. **Tracing and feature extraction of the PVD neuron**.

A A maximum projection image of the PVD neuron in a young-adult wild-type *C. elegans* expressing fluorescent Kaede. A=anterior, P=posterior, D=dorsal, V=ventral.

B A characteristic 'menorah' structure, a repetitive pattern in the PVD's dendritic arbor.

C A diagram of the menorah showing the conventional classification into branch orders.

D Outline of the algorithm for tracing and analysis of the PVD neuron. Starting with a grayscale image, a pre-trained convolutional neural network (CNN) is applied to increase the contrast between neuron and non-neuron pixels. The output of the CNN is binarized and skeletonized, and subsequently fed into the tracing algorithm to extract the precise neuronal structure. Finally, morphological features are extracted from the trace and quantified.

Figure 2. **Segmentation of the PVD using neural networks and active-contour models.**

A A denoising convolutional neural network (dnCNN) is trained to clean noisy image patches of small PVD elements, and increase the contrast between neuron and non-neuron pixels. The network gets a small image patch (top row, "Raw"), and returns an enhanced image of the same size (bottom row, "CNN").

B An illustration of the tracing process of a single neuronal segment. Sequential convolution of rectangles (green) is applied from the end-points inwards until the segment is fully traced.

C, D The local orientation of a PVD element (C) is determined by the optimal alignment of a rectangular mask (blue) with the dendritic process (white), corresponding to the maximal convolution score (D, dashed lines represent detected deviation angle).

E, F Apparent local width of a PVD element (E) found using the decay rate (second derivative) of the convolution function (F, dashed line represents detected apparent width), using the orientation found in (C-D).

G, H The intensity and variation of the local background are determined by sampling the pixels within rectangles on both sides of the one found in C-F (G, blue rectangles for the background and green for the dendritic process). These are used to normalize the score and account for variation in background throughout the image and across images. Statistics were calculated using the nonparametric Mann–Whitney test. ***$P < 0.0005$, **$P < 0.005$, *$P < 0.05$. Error bars show the standard deviation.

I-M Determining the geometry of neuronal junctions – center point, radius, and angles. Given an approximate center point from the skeleton image (red dot in J), the precise center is detected by optimally fitting a circular mask to the binarized dnCNN image (green dot in J). Following the detection of the precise center and radius (J), a radially aligned rectangular mask (blue) is convolved against the greyscale image (K). Peaks in the convolution function (L) correspond to the detected local junctional angles (α; M).

N An example of a fully traced wild-type PVD neuron (same neuron as Fig 1A). Yellow arrows indicate untraced segments.

Figure 3. The worm's coordinate system and PVD feature extraction.

A The coordinate system used to characterize the PVD neuron is defined by $\left(\hat{S},\hat{D},\hat{R}\right)$; where $\hat{S}$ is locally tangential to the worm's longitudinal axis, $\hat{D}$ points along the local dorsal direction, and $\hat{R}$ points in the direction of the worm's right.

B Using the projection image of the non-planar PVD neuron, an outline image is generated using morphological operations applied to the neuron's trace. This is used to find the neuron's centerline and borderline.

C A schematic of the worm's cross section. The azimuthal angle ϕ denotes the azimuthal position of PVD elements. r, radius at each point; d, distance.

D A schematic of the worm from a left/right side view. The angle θ denotes the orientation of PVD elements.

E, F Visualization of the azimuthal angle ϕ (E) and distribution of the PVD elements for different ϕ angles (F, n=11). The peaks at 0 and ±35° correspond to the primary (red) and tertiary (green, dorsal are positive and ventral are negative values) branches. Same neuron as Fig 1A.

G, H Visualization (G) and distribution (H) of orientation angle, θ, for PVD elements (n=11). The distribution shows that most of the neuron's length is either parallel (red) or perpendicular (green) to the midline. Dorsal and ventral D=dorsal, V=ventral, L=left, R=right, A=anterior, P=posterior.

Figure 4. **Morphological characterization of the wild-type PVD.**

A Distribution of PVD elements by the azimuthal angle, ϕ, and midline orientation angle θ. Four distinct morphological classes are found: Class 1 (red), class 2 (green), class 3 (blue) and class 4 (yellow) (n=11).

B The percentage of each of the morphological class found in (A); (n=11).

C Visual example of the algorithmically-derived classification (same neuron as Fig 1A)., closely resembling conventional branch-order classification scheme (see figure 1C)., .

D Distribution of neuron length elements along the midline, classified as in C and averaged across worms (n=11).

E Mean curvature of neuronal elements for each morphological class. Class 4 elements are the most curved, whereas class 3 elements are more curved than class 1 and 2, but less than 4. Statistics were calculated using the nonparametric Mann–Whitney test. ***P < 0.0005, **P < 0.005, *P < 0.05. Error bars show the standard deviation (n=11). Same neuron as Fig 1A.

F Example of a PVD neuron color-coded for curvature . Same neuron as Fig 1A.

Figure 5. **The geometry of PVD junctions.**

A Examples of various PVD junction morphologies. Colors correspond to relative junctional angle size: smallest (red, α_1), mid-size (green, α_2) and largest (blue, α_3).

B Each junction is described by three angles, corrected for distortion due to projection. The distributions of the smallest (red), mid-size (green) and largest (blue) angles are shown (n=11 animals; 2853 junctions). The mean values of the angle distributions are 85°, 119° and 156°.

C A cartoon showing the effect of random variations in junction configuration. An intrinsic junction configuration (top) is deformed, resulting in one of the possible deformed configurations (bottom).

D Fit of Monte Carlo simulated angle distributions with the experimental distributions. The best fit to the experimental data is for a symmetrical configuration with a standard deviation of σ_α =19° around the mean values ({α_1=120°, α_2=120°, α_3=120°, σ_α=19°}; configuration (4)). Circled numbers correspond to the simulation examples in (E).

E Examples of simulated junction configurations. Circled numbers correspond to the ones in (D) to show the residual error for each simulation. Solid lines indicate probability densities for simulated junctions, bars indicate frequencies from experimental data. (1)={α_1=90°,α_2=90°,α_3=180°,σ_α=26°}, (2)={α_1=80°, α_2=130°, α_3=150°, σ_α=17°}, (3)={α_1=94°, α_2=118°, α_3=148°, σ_α=15°}, (4)={α_1=120°, α_2=120°, α_3=120°, σ_α=19°}. Configuration (4) gives the best fit as shown in (D).

Figure 6. **Distributions of geometrical PVD elements in wild-type and *git-1* mutant.**

A An image of a full PVD of a *git-1* mutant, superimposed with color-coded morphological classes: red - class 1, green - class 2, blue – class 3, yellow – class 4.

B Total PVD length for each morphological class for WT (blue) and *git-1* mutant (red), normalized to the PVD midline length.

C The length density of junctions along the dendritic processes (reciprocal of the average length of dendrites between junctions), for each morphological class

D The length density of tips along the dendritic processes for each morphological class.

E The number of dendritic tips, normalized to midline length of the PVD, for each of the four morphological classes.

F-I Magnified regions of typical PVD morphologies in wild-type (F-G) and *git-1* (H-I). Arrows show abnormal branching in *git-1* compared to wild-type. This includes excess of junctions and tips, as well as neuronal processes that do not follow the pattern

described in figures 3 and 4. Dendritic segments color-coded according to classification: red - class 1, green - class 2, blue – class 3, yellow – class 4.

In B-E, statistics were calculated using the nonparametric Mann–Whitney test. ***$P < 0.0005$, **$P < 0.005$, *$P < 0.05$. 11 Wild-type animals, with 2853 junctions and 2916 tips. 10 *git-1* animals, with 10, 2621 junctions and 2608 tips. Bars show the mean value and error bars show the standard deviation.

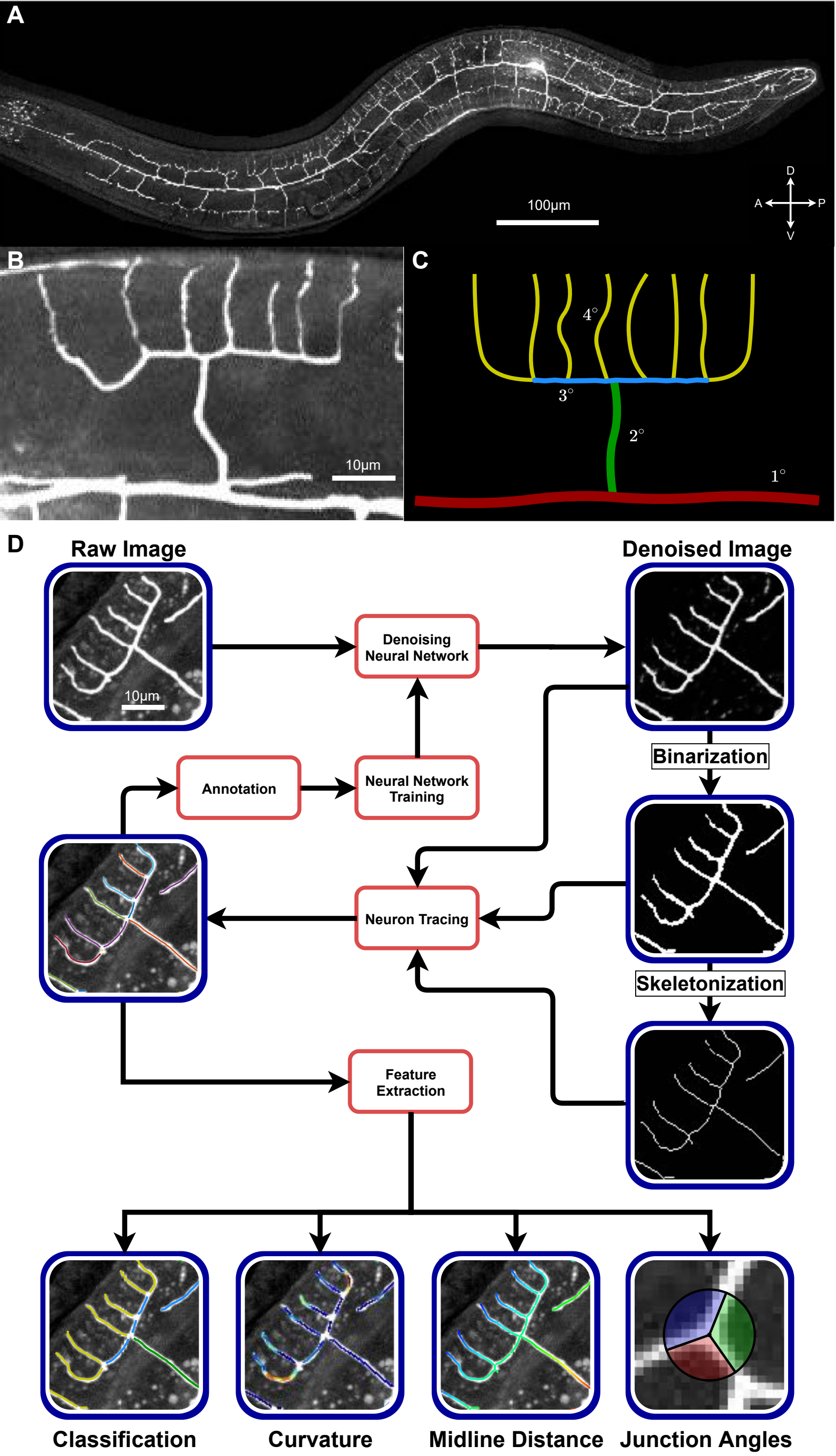
A
100µm
D
A
P
V
B
10µm
C
4°
3°
2°
1°
D
Raw Image
10µm
Denoising Neural Network
Denoised Image
Binarization
Annotation
Neural Network Training
Neuron Tracing
Skeletonization
Feature Extraction
Classification
Curvature
Midline Distance
Junction Angles

Figure 1

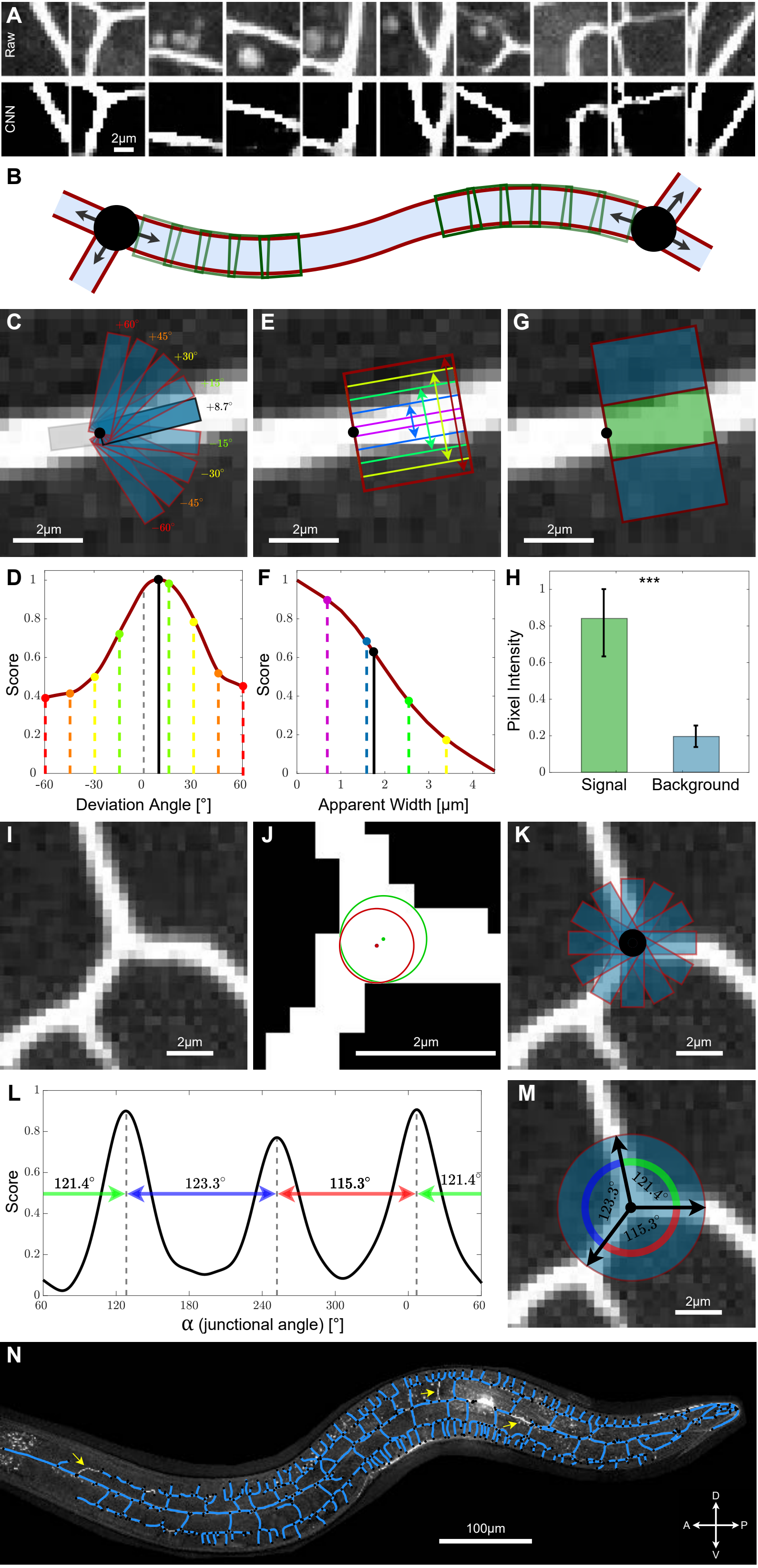
A
Raw
CNN
2µm
B
C
+60°
+45°
+30°
+15°
+8.7°
−15°
−30°
−45°
−60°
2µm
E
2µm
G
2µm
D
Score
Deviation Angle [°]
F
Score
Apparent Width [µm]
H
***
Pixel Intensity
Signal
Background
I
2µm
J
2µm
K
2µm
L
Score
121.4°
123.3°
115.3°
121.4°
α (junctional angle) [°]
M
121.4°
123.3°
115.3°
2µm
N
100µm
D
A
P
V

Figure 2

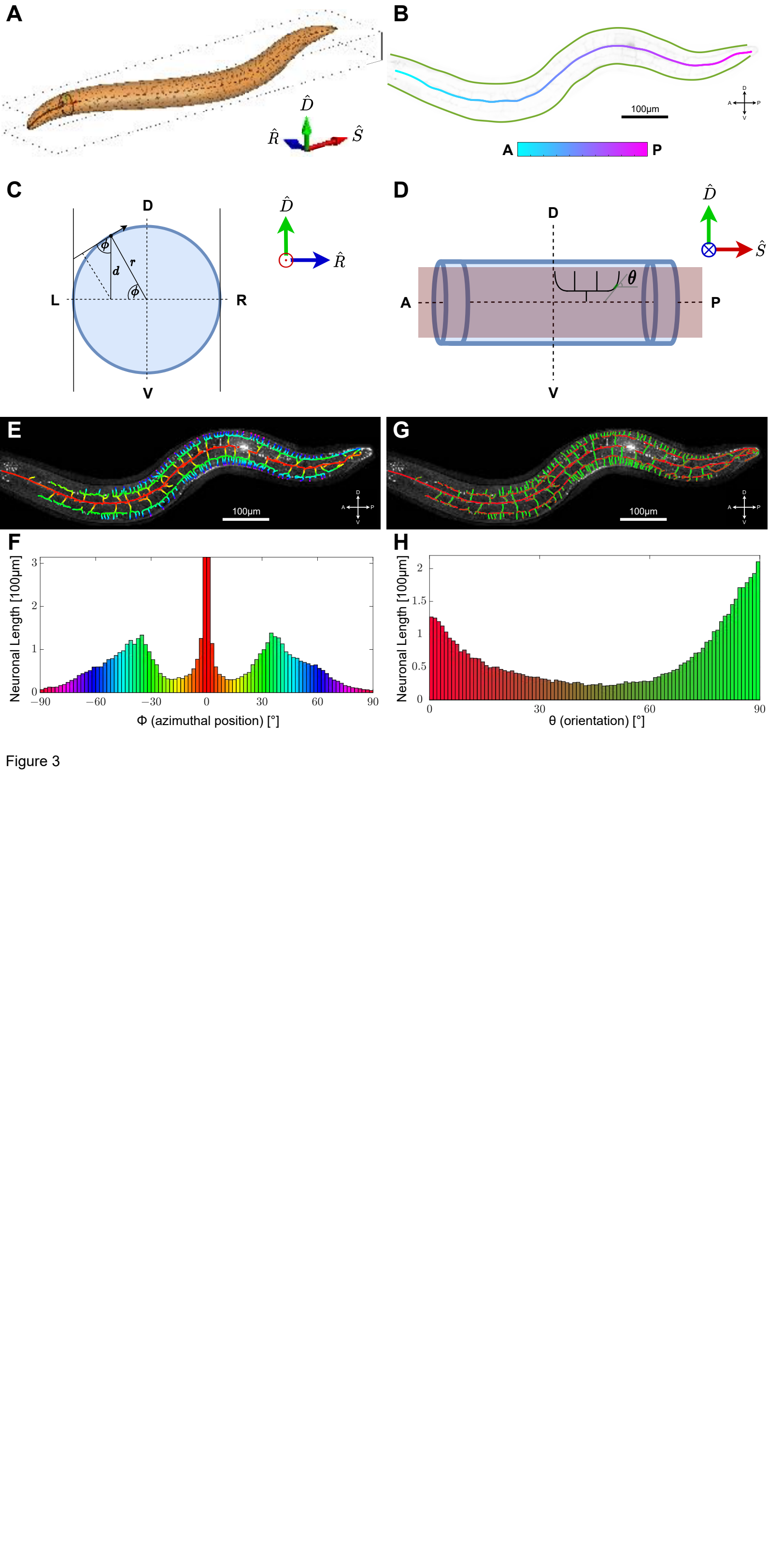
A
$\hat{D}$
$\hat{R}$
$\hat{S}$
B
100µm
A
P
C
D
L
R
V
ϕ
d
r
$\hat{D}$
$\hat{R}$
D
$\hat{D}$
$\hat{S}$
θ
A
P
V
E
100µm
G
100µm
F
Neuronal Length [100µm]
Φ (azimuthal position) [°]
H
Neuronal Length [100µm]
θ (orientation) [°]

Figure 3

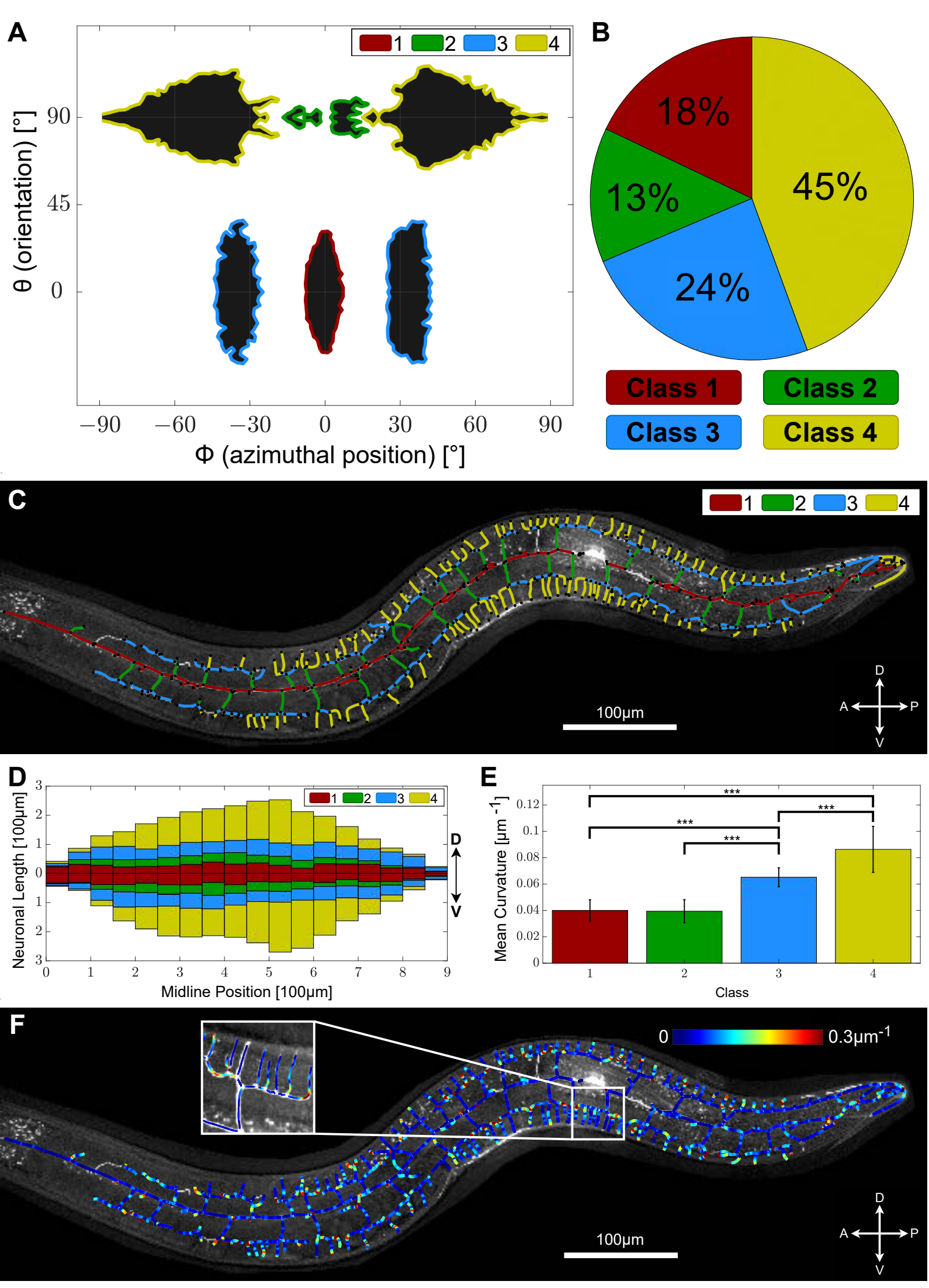
A
1
2
3
4
θ (orientation) [°]
90
45
0
−90
−60
−30
0
30
60
90
Φ (azimuthal position) [°]
B
18%
13%
24%
45%
Class 1
Class 2
Class 3
Class 4
C
1
2
3
4
100µm
D
A
P
V
D
Neuronal Length [100µm]
Midline Position [100µm]
E
Mean Curvature [µm -1]
Class
***
F
0
0.3µm-1
100µm
D
A
P
V

Figure 4

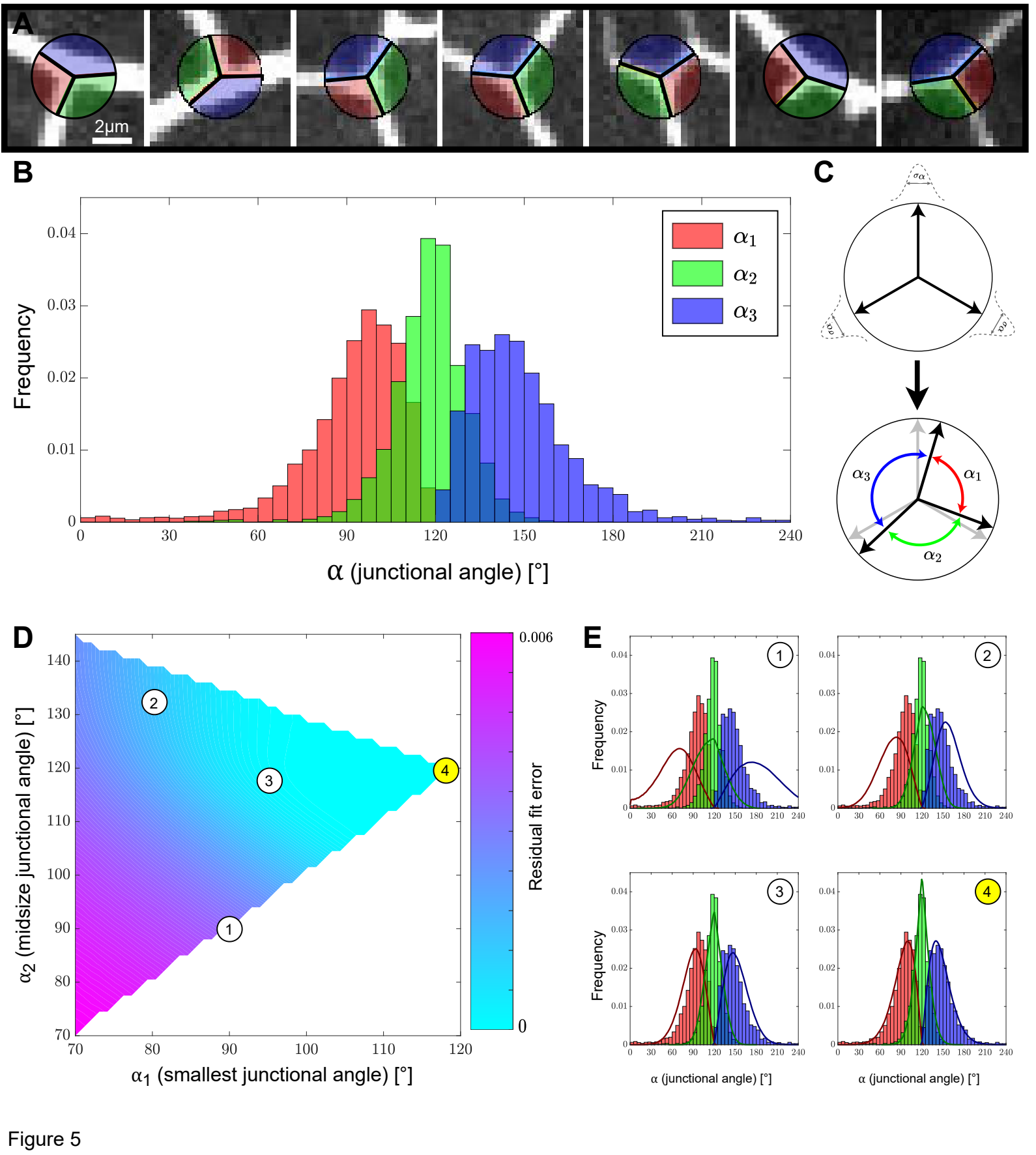
A
2µm
B
Frequency
α (junctional angle) [°]
α_1
α_2
α_3
C
D
α_2 (midsize junctional angle) [°]
α_1 (smallest junctional angle) [°]
Residual fit error
0.006
0
E
Frequency
α (junctional angle) [°]

Figure 5

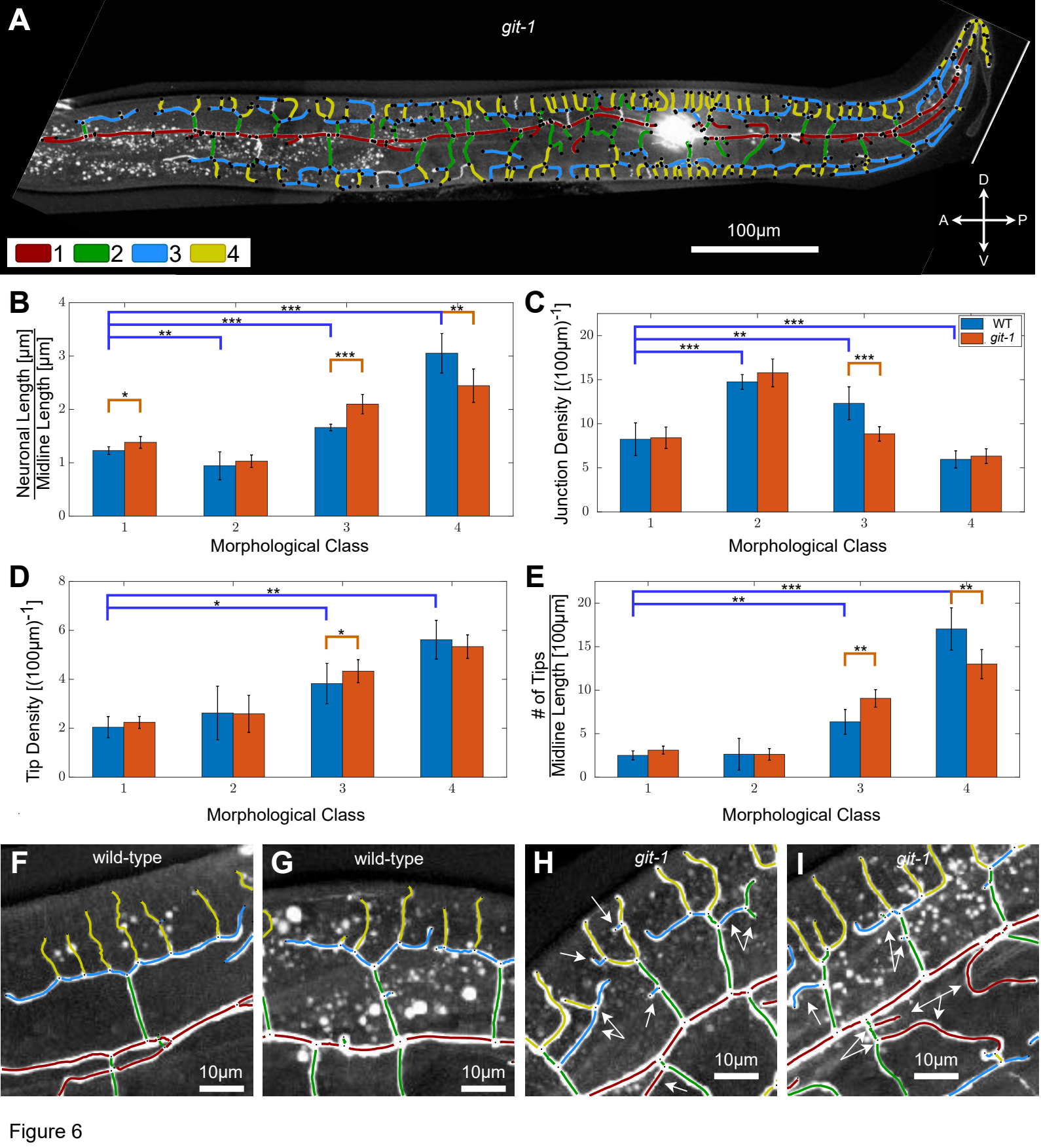
A
git-1
1
2
3
4
100µm
D
A
P
V
B
Neuronal Length [µm] / Midline Length [µm]
Morphological Class
C
Junction Density [(100µm)^-1]
WT
git-1
Morphological Class
D
Tip Density [(100µm)^-1]
Morphological Class
E
# of Tips / Midline Length [100µm]
Morphological Class
F
wild-type
10µm
G
wild-type
10µm
H
git-1
10µm
I
git-1
10µm

Figure 6